Asian Journal of Chemistry; Vol. 32, No. 11 (2020), 2763-2772

ASIAN JOURNAL OF CHEMISTRY

https://doi.org/10.14233/ajchem.2020.22845

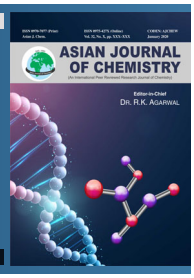

Influence of Fe and Ni Doped CuO Nanomaterials for High Performance Supercapacitors

PALANISAMY REVATHI[1], VENKATACHALAM MANIKANDAN[1], PANNEERSELVAM EZHILMATHI[1], VEERASAMY UMA SHANKAR[2], PALANI SUGANYA[1] and KUPPUSAMY KRISHNASAMY[1,*]

[1]Department of Chemistry, Annamalai University, Annamalainagar-608002, India
[2]Department of Physics, Annamalai University, Annamalainagar-608002 India

*Corresponding author: E-mail: krishnasamybala56@gmail.com

Received: 2 June 2020; *Accepted*: 4 July 2020; *Published online*: 28 October 2020; AJC-20099

This paper focuses on the synthesis of doped and undoped CuO nanoparticles using the sol-gel method, which has been prepared and described. Supercapacitor applications of as-synthesized nanomaterials were analyzed using cyclic voltammetry (CV), galvanostatic discharge (GCD) and electrochemical impedance spectroscopic (EIS) analysis. The cyclic voltammograms illustrated the quasi-rectangular shape which depicted the pseudocapacitance nature of the samples. The calculated specific capacitance of the prepared samples was 180, 253 and 303 (F/g) corresponding to CuO, Fe-CuO and Ni-CuO, respectively at the low current density and the EIS spectra show that the prepared Ni-CuO electrode exhibits low charge transfer resistance.

Keywords: CuO nanoparticles, Doped CuO, Sol-gel method, Pseudocapacitance.

INTRODUCTION

Nowadays the energy requirement and demands are rapidly increased hence many of the researchers put lot of efforts to develop the high-performance energy storage devices. As a sort of energy storage device, supercapacitors have its selective properties like quick charge-discharge rate, high power density and stable cycling performance [1-3].

As well known, the supercapacitors are highly depends on the properties of electrode materials. So, it is essential to prepare the good cathode materials for the better electrochemical performance which increase the specific capacitance and energy density for the supercapacitors [4-7]. Based on the literature survey, transition metal elements like, Ni [8], Zn [9], W [10], Ru [11], Mn [12], Fe [13-16] and its oxide source elements are selected as materials for high performance supercapacitance applications. Among these, copper oxide (CuO) has attractive material in recent years because of its low cost, abundant resources, high energy density, *etc*. It is a key component in high superconductors and used as photoconductive material [17-19]. Nasir *et al*. [20] reported that NiO/CuO nanocomposites achieved a capacitance values 280 F g^{-1} at 1 A g^{-1} in 6M KOH. A rose like CuO was easily prepared by chemical deposition method and reported as an higher specific capacitance material (284 F g^{-1} at 0.5 mA cm^{-2}) in 1M KOH solution [21]. The CuO nanoplates was prepared by chemical method using 6M KOH as an electrolyte solution [22], which acted as the supercapacitance material having a value of 536 F g^{-1} at 2 A g^{-1}. Spindle like CuO nanomaterials was prepared by co-precipitation method at the specific capacitance value of 130 F g^{-1} at 1 A g^{-1} for an electrolyte solution of 0.5 M K_2SO_4 [23].

Transition metals (Ni, Mn, Fe, Cd and Zn) doped CuO was reported by few researchers to improve the electrochemical performance of CuO [24-27]. Several modified chemical and physical methods such as sol-gel, hydrothermal, chemical, combustion, electrochemical, sonochemical and coprecipitation methods were developed for obtaining the CuO nanoparticles [28,29]. Hence in this present work, an attempt has been made to synthesize and characterize CuO and Fe, Ni-doped CuO nanoparticles using sol-gel method and its electrochemical performances were analyzed.

EXPERIMENTAL

Synthesis of CuO and Fe, Ni doped CuO nanoparticles: The CuO nanoparticles was synthesized by sol-gel method.

In brief, copper(II) chloride (5 mM) dissolved in 100 mL of distilled water, then 20 mM NaOH was slowly added and stirred for 3 h at 70 ºC. The obtained black precipitate was rinsed by deionized water and ethanol for several times and dried at 90 ºC for 14 h. Finally, the precursor was calcined at 550 ºC for 4 h. Further ferric chloride and nickel chloride was introduced into the same procedure to obtain the Fe and Ni doped CuO nanomaterials.

Preparation of electrode: The working electrodes were fabricated by mixing the active material, acetylene black and polyvinylidene difluoride(PVDF) as a binder (weight ratio of 7:2:1 v/v%) and *N*-methyl-2-pyrrolidone used as a solvent. The semi-liquid paste have been coated on Ni plate as a current collector and the electrodes were dried at 110 ºC for overnight. In this electrochemical cell arrangement, 1 M KOH solution was used as an electrolyte. The reference and counter electrodes consisted of Ag/AgCl and inert platinum, respectively.

Characterization: The XRD study of the synthesized pure and Fe, Ni -doped nanoparticles was performed using Rigaku-Ultima IV in the 2θ range from 10-80º at room temperature at a scanning rate of 10º/min. The X-ray diffractometer was operated at 30 mA, 40 kV for the Cu*K*α line to identify the crystal structure. The morphological and size distribution were characterized using SEM technique and the elemental mapping study was confirmed (Bruker) the presence of Cu, Fe, Ni and O elements with their extend of distribution. The optical absorption studies were carried out using UV-Vis spectrometer (Jasco, V-650) in the wavelength range from 200 to 1100 nm. The photoluminescence (PL) spectra were recorded at room temperature (Fluro Max-4L) with a maximum power output of 10 mW. Fourier transform infrared spectra of the synthesized samples were recorded using a Perkin-Elmer Spectrometer (Model-RXI) using KBr pellet in the range of 4000-400 cm^{-1}. The cyclic voltammetry (CV), galvanostatic charge discharge (GCD) and electrochemical impedance spectroscopy (EIS) analysis were characterized through CH066-instrument to study the pseudocapacitance behaviours.

RESULTS AND DISCUSSION

Structural analysis: The XRD patterns of CuO, Fe and Ni doped CuO nanoparticles are shown in Fig. 1. The sharp peaks in the spectra indicated that the products were well crystalline nature. The characteristic peaks located at 2θ = 31.62º, 34.65º, 37.85º, 39.67º, 57.75º, 60.55º, 67.27º and 74.13º, which correspond the (110), (002), (111), (200), (202), (113), (220) and (004) planes, respectively oriented with the tetragonal phase of the CuO (JCPDS 89-2531). The XRD patterns of the Fe and Ni doped CuO showed a slight deviation in the XRD angles with respect to the pure CuO indicated that the doping of metal ions not influenced on the phase transition. Also, all the diffraction features were indexed to the tetragonal structure. The crystallite size of the pure CuO and Fe, Ni doped CuO samples were calculated by using the following Scherrer′s relation (eqn. 1):

$$D = \frac{n\lambda}{\beta\cos\theta} \quad (1)$$

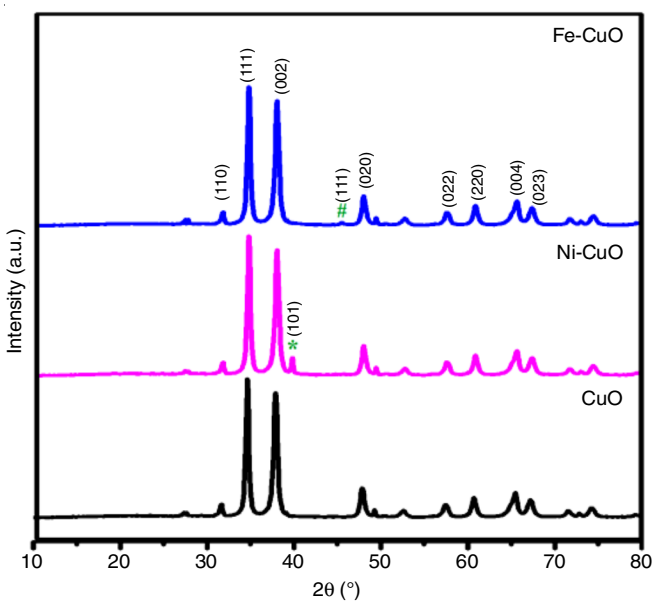

Fig. 1. X-ray diffraction pattern of CuO, Fe doped CuO and Ni doped CuO

where D is the average size, 'n' is the Scherrer constant (0.9), λ is the wavelength of the incoming X-rays (1.54060 Å for Cu*K*α), d is the lattice space, δ is the diffraction angle and β is the full width half maximum. The calculated average crystalline size of the pure and Fe, Ni doped CuO is shown in Table-1. The average crystallite size of the pure CuO and Fe and Ni doped CuO samples were found to be 33.72, 21.49 and 19.6 nm. This result shows that the CuO nanoparticles crystallite size was greater than the Fe and Ni doped CuO nanoparticles due to the substitution of lesser ionic radius of Fe (0.64 Å) and Ni (0.69 Å) to the space of Cu (0.73 Å) atom. The other structural parameters like dislocation density (δ), stacking fault (SF) and micro strain (ε) were also calculated from the XRD results using eqns. 2-4.

$$\text{Dislocation density } (\delta) = \frac{1}{D^2} \quad (2)$$

$$\text{Stacking fault } (SF) = \left(\frac{2\pi^2}{45(\tan\theta)^{1/2}}\right)\beta \quad (3)$$

$$\text{Micro strain } (\varepsilon) = \frac{\beta(\cos\theta)}{4} \quad (4)$$

TABLE-1
STRUCTURAL PARAMETERS OF CuO, Fe AND Ni DOPED CuO

Samples	Crystalline size (nm)	Dislocation density (δ) (10^{-15})	Micro strain (ε) (10^{-3})	Stacking fault
CuO	33.72	0.86	2.15	0.098
Fe-CuO	21.49	2.16	2.84	1.534
Ni-CuO	19.16	2.72	4.13	0.124

The dislocation density and microstrain values increase for the Fe and Ni doped CuO samples than the pure CuO, indicated that the crystalline size is inversely related to dislocation density and microstrain parameters [30].

SEM analysis: The SEM images of CuO, Fe and Ni doped CuO are presented in Fig. 2. The SEM image of CuO (Fig. 2a) sample shows the existence of uniform rod like shape nanoparticles with the small agglomeration. The SEM images of the Fe and Ni doped CuO are given in Fig. 2c and 2e, respectively and the images revealed that some doped particles are decorated on the surface of CuO [31]. The EDX spectra of CuO, Fe-CuO and Ni-CuO are also illustrated in Fig. 2(b, d & f), which confirm the presence of Cu, O, Fe and Ni in the prepared samples.

The element mapping of the synthesized materials is shown in Fig. 3(a-c) and the presence of the dopant concentration were confirmed from the element mapping images. The extend of distribution of copper, oxygen, iron and nickel in the prepared nanomaterials are reproduced in Fig. 3d-g. The element mapping images further indicated that the doping process of iron is carried out smoothly than the nickel.

UV-visible analysis: UV-visible absorption spectra of CuO and Fe and Ni-doped CuO nanostructure is displayed in Fig. 4. It can be seen that the absorption reaches the highest point (λ_{max}) for undoped CuO at 326 nm and the λ_{max} value shifted towards the higher wavelength region such as 333, 349 nm for Fe and Ni doped CuO. This red shift indicated the incorporation of Fe^{2+} and Ni^{2+} ions into the CuO lattice. The optical band gap value was calculated using the eqn. 5.

$$E_g = h\nu = \frac{hc}{\lambda} \quad (5)$$

The bandgap values have been determined for CuO (3.8 eV), Fe-CuO (3.7 eV) and Ni-CuO (3.5 eV) and the values have shown that the energy gap of Fe and Ni-doped CuO has been slowly decreased relative to the undoped CuO and has a red-shift due to the contribution of Fe and Ni orbitals to both

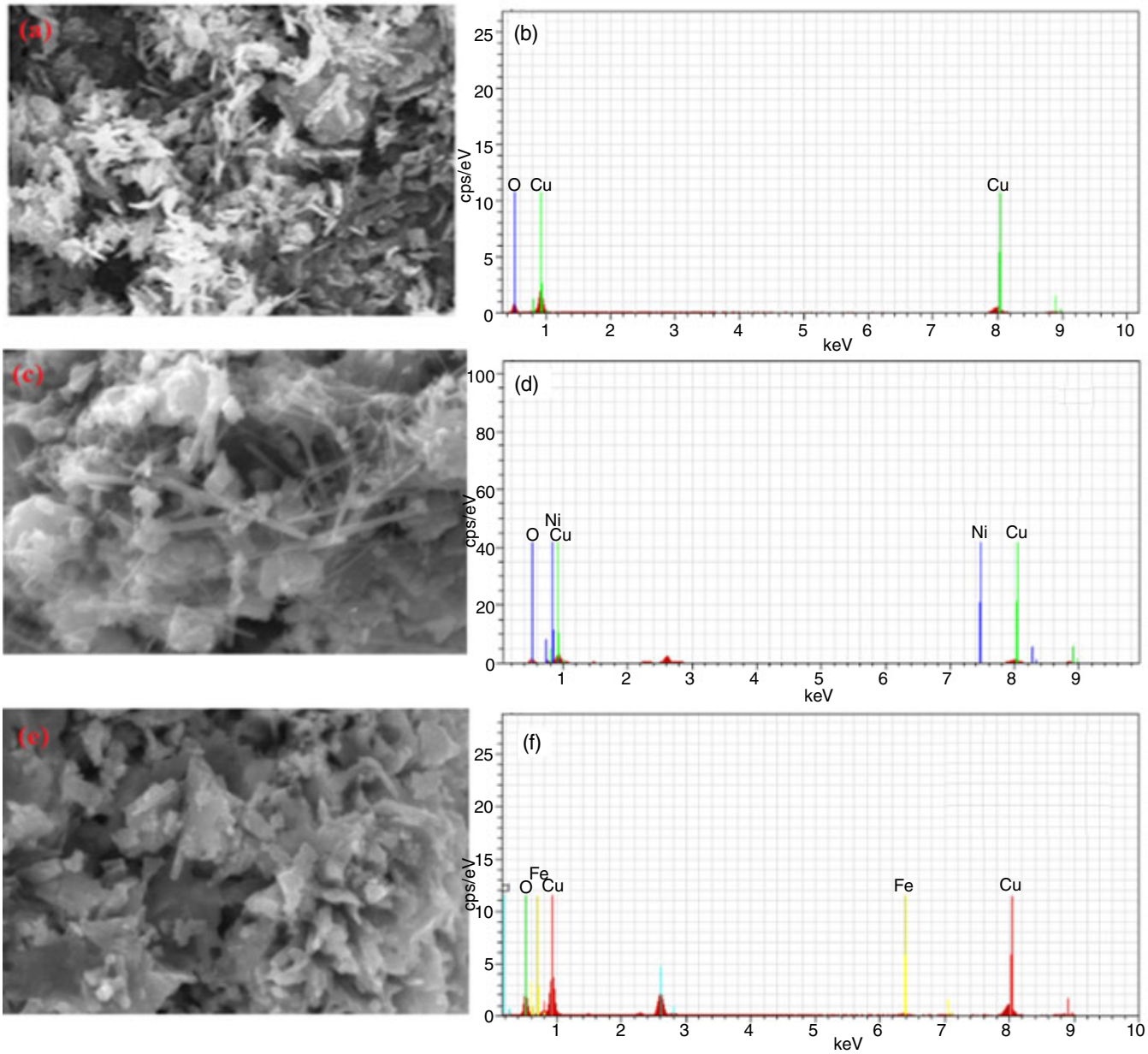

Fig. 2. SEM Images and EDX spectra of (a, b) CuO, (c, d) Fe doped CuO and (e, f) Ni doped CuO

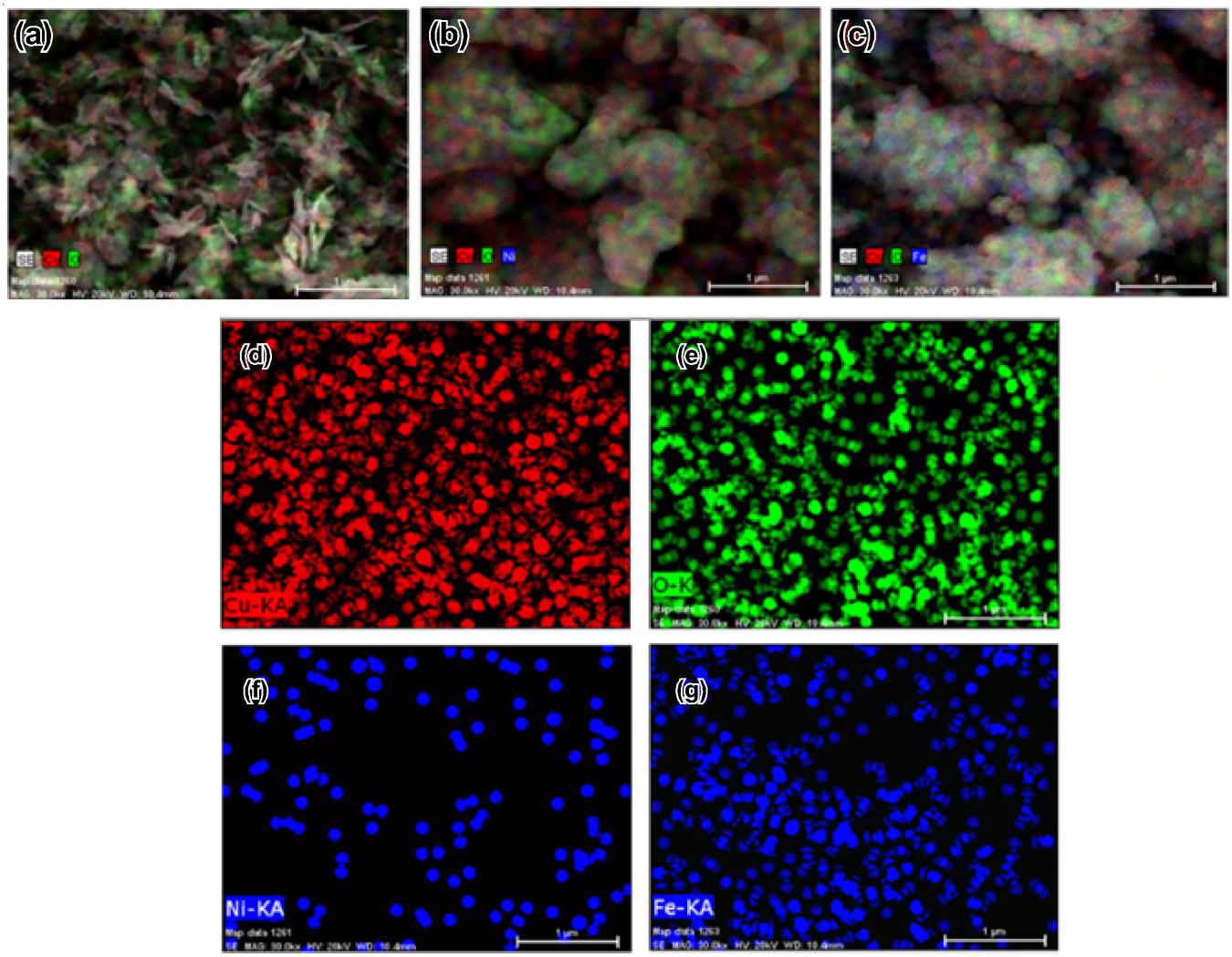

Fig. 3. Element mapping of (a) CuO, (b) Fe doped CuO, (c) Ni doped CuO and (d-g) Element distribution of Cu, O, Ni and Fe

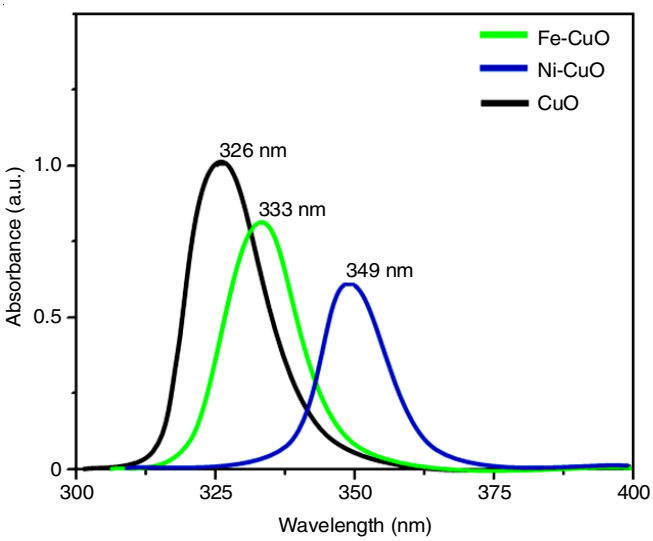

Fig. 4. Absorption spectra of CuO, Fe and Ni doped CuO

valence and conduction bands [32-36]. The crystalline size was primarily expressed in the magnitude of the band gap as with the inverse relationship.

FTIR analysis: FT-IR spectra of pure and Fe, Ni doped CuO nanoparticles are shown in Fig. 5. The absorption peaks observed at 3396 cm^{-1} (pure CuO), 3332 cm^{-1} (Fe-CuO) and

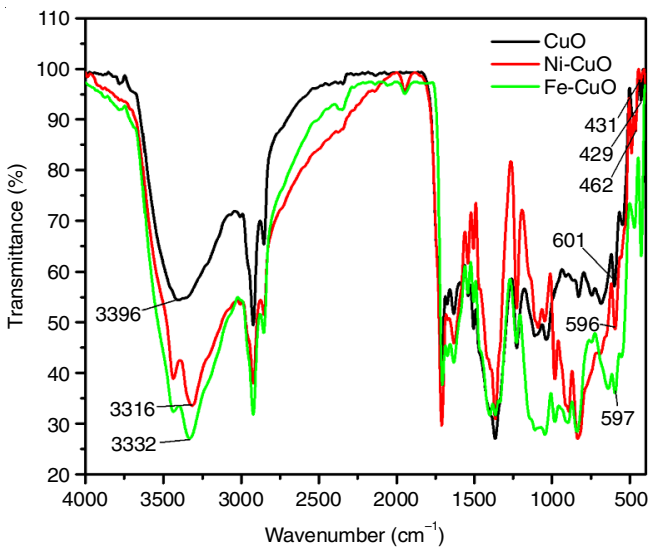

Fig. 5. FT-IR spectra of CuO, Ni doped CuO and Fe doped CuO

3316 cm^{-1} (Ni-CuO) are responsible for the adsorbed water molecules on the metal surface. The band located at 1632 cm^{-1} referred to the bending and stretching vibrations of -OH group as certained the adsorption of water on the surface of nanomaterials. The absorption bands at 601 and 429 cm^{-1} are assigned for Cu-O stretching vibrations. In the Fe and Ni doped CuO nanoparticles, these stretching vibrations are slightly shifted from 597 to 428 cm^{-1} for Fe-CuO and 596 to 431 cm^{-1} for Ni-CuO confirmed the occupation of Fe and Ni ions on the CuO host lattice. These observed metal-oxide stretching modes confirmed the successful incorporation of Fe and Ni ions into the host lattice of CuO.

XPS analysis: XPS spectra of Fe-CuO and Ni-CuO are shown in Fig. 6. As seen in Fig. 6a-b, the wide XPS spectra

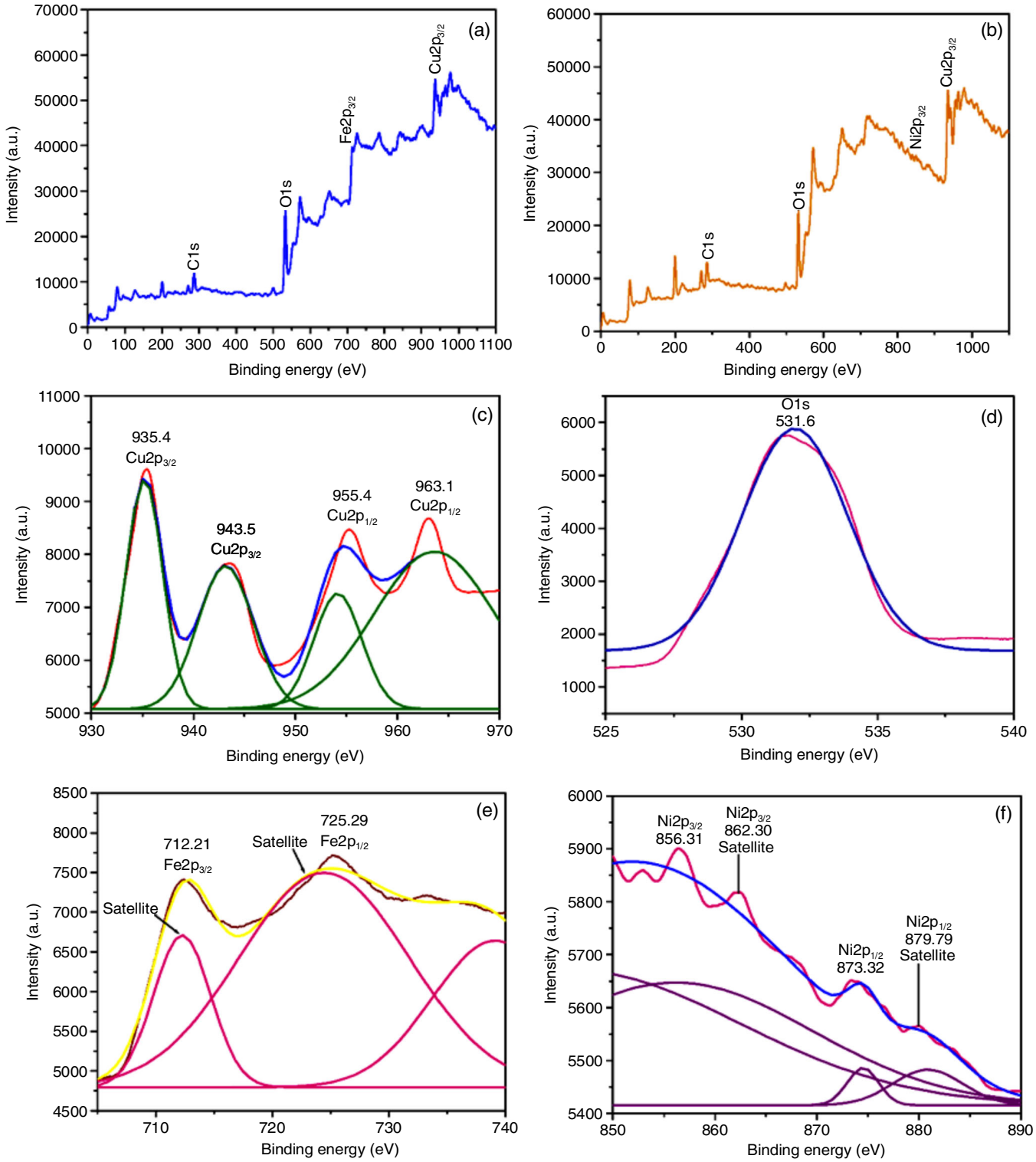

Fig. 6. XPS survey spectrum of Fe-CuO, Ni-CuO(a, b), (c) Core level spectrum of Cu 2p state, (d) O1s core level spectrum and (e, f) core level spectrum of Fe 2p and Ni 2p nanoparticles

revealed the presence of Cu, O, C, Fe and Ni elements in the samples. In the XPS spectra, appearance of carbon is common [37,38]. Fig. 6e-f illustrates the de-convoluted curves of Cu, O, Fe and Ni elements. The peaks observed at 963 and 936 eV corresponding to Cu-$2p_{1/2}$ and Cu-$2p_{3/2}$, which evidently shows the presence of Cu^{2+} ions (Fig. 6c). The energy separation between the Cu^{2+} ion is 19.9 eV. The peak appeared at 531 eV corresponds to O-1s in the lattice (Fig. 6d) [39]. The peaks located at 712.21 and 725.29 eV (Fig. 6e) correlated to Fe-$2p_{3/2}$ and Fe-$2p_{1/2}$, respectively, which originated from Fe^{3+} ion [40]. The core-level spectrum of Ni-2p (Fig. 6f) shows the peak values at 856.51 and 879.9 eV attributed to Ni-$2p_{3/2}$ and Ni-$2p_{1/2}$, respectively [41]. These values are in good agreement with the previous report [42]. The XPS results proved that there has been a strong interaction between dopent and CuO nanoparticles.

Cyclic voltammetry: The CV curves of CuO, Fe-CuO and Ni-CuO electrodes at different scan rates like 10, 20, 50 and100 mV/s with a potential window range from – 0.6 to + 1.0 V in 1M KOH electrolyte solution is shown in Fig. 7. From the cyclic voltammograms, all the CuO derivative electrodes exhibited an almost rectangular shape (Fig. 7). The CV curve current was increased by increasing the scan rate as observed in Fig. 7a. At a lower scanning rate, protons or K^+ ions may have more time to reach the surface of the electrode. At a higher scan rate, the time available for the K^+ ions integrated into the electrode is inadequate. A linear relationship was observed between the peak current and the square root of scan rates ($v^{1/2}$) of pure CuO, Fe-CuO and Ni-CuO electrodes (Fig. 7d). From Fig. 7d, with increasing the scan rate the reductive peak shifted towards negative and oxidative peak move towards more positive potential regions.

Moreover, the Ni-CuO electrode has the evasive peak than Fe-CuO and pure CuO, which suggest that the Ni ion provides a larger area to improve the conductivity of the CuO. The specific capacitance of the CuO, Fe-CuO and Ni-CuO electrode materials were calculated with the scan rate (Table-2) by using eqn. 6 [43-45]:

$$C_s = \frac{s}{mk\Delta V} \quad (6)$$

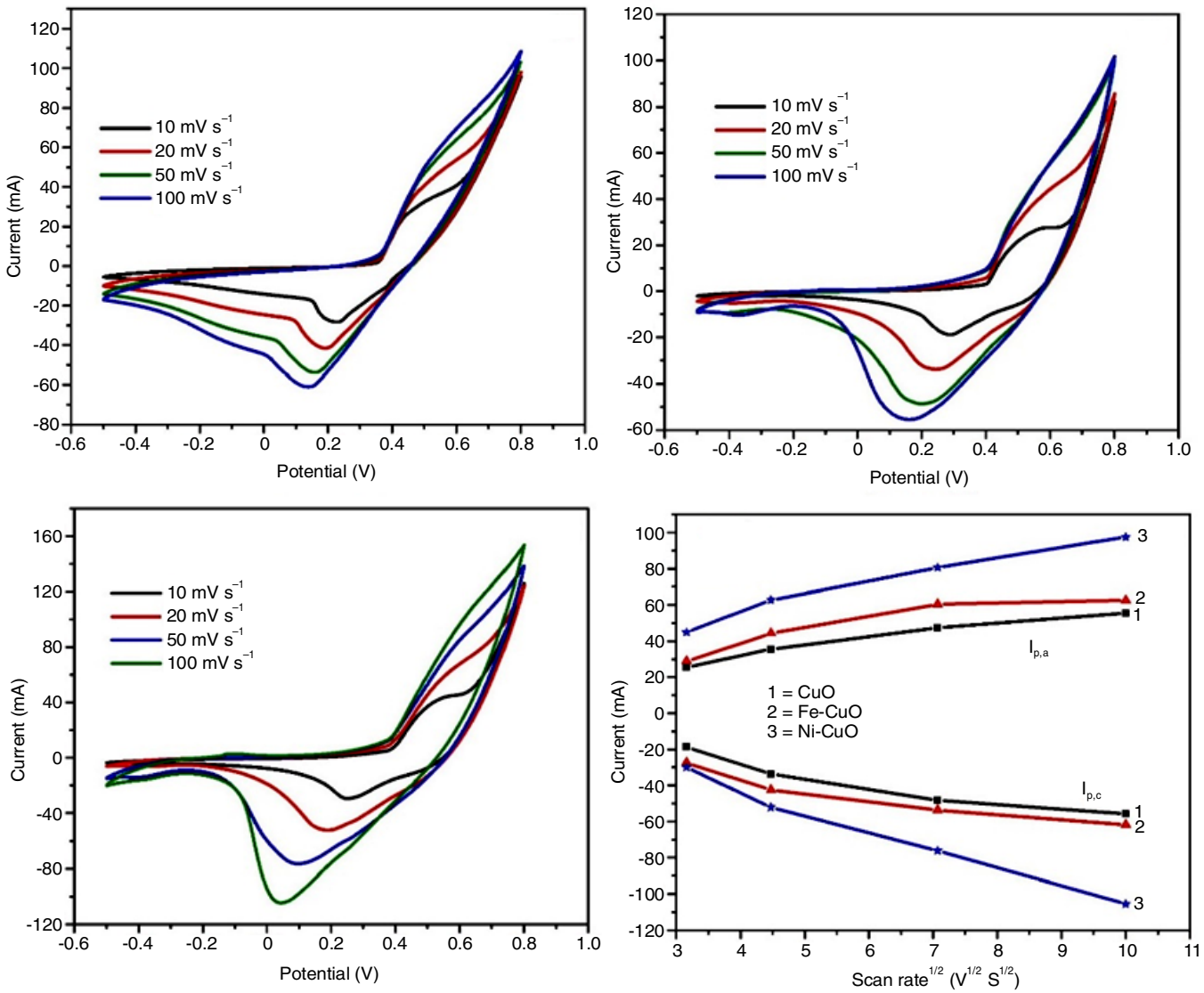

Fig. 7. CV curves of (a) CuO (b) Fe-CuO (c) Ni-CuO and (d) Peak to peak separation of CuO, Fe-CuO and Ni-CuO electrodes

where C_s is the specific capacitance of the active electrode material, S is the specific area of the CV curve, m is the mass of the electrode, k is the scan rate and ΔV is the potential window. From Table-2, Ni-CuO electrode exhibited the much higher specific capacitance value than the Fe-CuO and CuO electrodes. The Ni-CuO electrode capacitance value was roughly two-fold greater than the pure CuO and Fe-CuO electrodes. Also, the specific capacitance of bare CuO electrode has the capacitance retention at 51% at the higher scan rate whereas the Fe-CuO and Ni-CuO electrodes have exhibited the capacitance retention upto 60% and 64% which support the good electrochemical stability of the Ni-CuO electrode.

TABLE-2
SPECIFIC CAPACITANCE VALUES OF CuO, Fe DOPED CuO AND Ni DOPED CuO

Scan rate ($mV\ s^{-1}$)	Specific capacitance (F/g)		
	CuO	Fe-CuO	Ni-CuO
10	201.21	213.48	256.82
20	168.68	200.87	237.48
50	134.66	156.19	181.23
100	102.51	129.4	142.51

Fig. 8 shows the relation between specific capacitance and $v^{1/2}$ for CuO, Fe-CuO and Ni-CuO electrodes. It can be seen that the specific capacitance decreased with an increase in the scan rate from 10 to 100 mV s^{-1} due to the lesser time available for ion diffusion and adsorption inside the smallest pores within a huge particle at high scan rates [46]. The relation between specific capacitance with square root of scan rate indicated that Ni-CuO electrode has shown superior capacitance performance than the CuO and Fe-CuO electrodes.

The galvanostatic charge discharge (GCD) curves of CuO, Fe-CuO and Ni-CuO electrodes were recorded at 5 and 10 A g^{-1} in 1 M KOH electrolyte solution. The shape of the GCD curves are symmetrical triangular nature (Fig. 9) and the GCD curves had large time responds at low current density due to low internal resistance, which represents the adequate inclusion

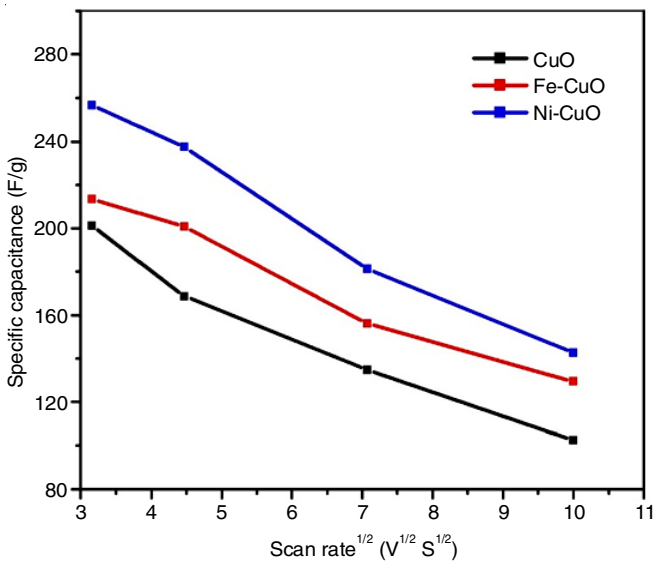

Fig. 8. Relation between specific capacitance and the square root of scan rates ($v^{1/2}$)

or exclusion of K^+ during the charging/discharging action. The specific capacitance can be calculated from the GCD curve using eqn. 7:

$$C_p = \frac{I\Delta t}{m\Delta V} \quad (7)$$

where, C_p is the specific capacitance (F g^{-1}), I is the discharge current (A), Δt is the discharge time period, m is the mass of the electrode and ΔV is the potential window. The specific capacitance for CuO, Fe-CuO and Ni-CuO were 180, 253 and 303 F g^{-1}, respectively at the current density of 5 A g^{-1}. The calculated specific capacitance values were decreased when increase in current density due to the incremental voltage drop fall and inadiquate active material associated with the redox reaction [47,48]. The specific capacitance values of different morphological CuO nanocyrstallites are given in Table-3. Among the various nanomaterials, the Ni/CuO electrode has

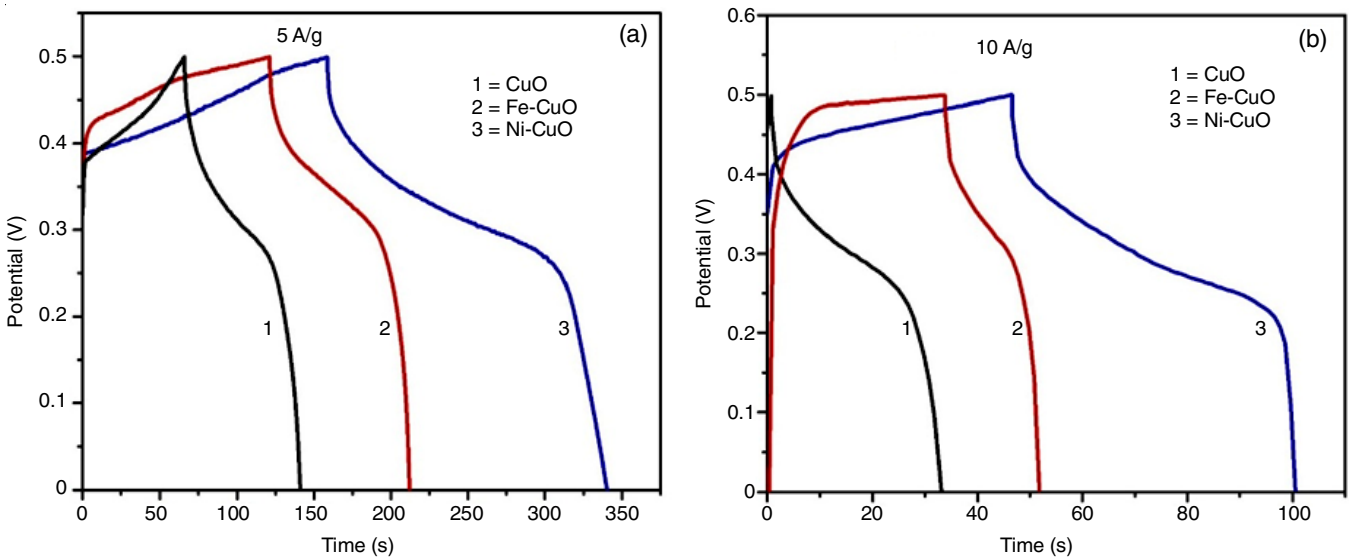

Fig. 9. Galvanostatic charge discharge (GCD) curves of bare, Fe-CuO and Ni-CuO nanoparticles

TABLE-3
COMPARISON OF THE SUPERCAPACITOR PERFORMANCE OF CuO, Fe-CuO AND Ni-CuO NANOPARTICLES

Synthetic method	Electrode material	Specific capacitance	Electrolyte	Ref.
Sol-gel	CuO nanorod	180 Fg^{-1}@ 5 Ag^{-1}	1 M KOH	Present work
Sol-gel	Fe-CuO nanorod	253 Fg^{-1}@ 5 Ag^{-1}	1 M KOH	Present work
Sol-gel	Ni-CuO nanorod	303 Fg^{-1}@ 5 Ag^{-1}	1 M KOH	Present work
Hydrothermal	NiO/CuO composite	280 Fg^{-1} @ 1 Ag^{-1}	6 M KOH	[40]
Chemical deposition method	Rose like CuO	284 Fg^{-1}@ 0.5 mA cm^{-2}	1 M KOH	[42]
Co-precipitation method	Spindle like CuO	130 Fg^{-1}@ 1 Ag^{-1}	0.5 M K_2SO_4	[23]

shown appreciable super capacitance efficiency. Furthermore, the energy density and power density values were calculated using eqns. 8 and 9.

$$E = \frac{1}{2}CV^2 \quad (8)$$

$$P = \frac{E}{t} \quad (9)$$

where, E and P are the energy and power densities of the electrode, C is the specific capacitance, t is the discharging time and V is the potential window. Fig. 10 shows the Ragone plot of CuO, Fe-CuO and Ni-CuO electrode materials. The calculated E and P values are given in Table-4.

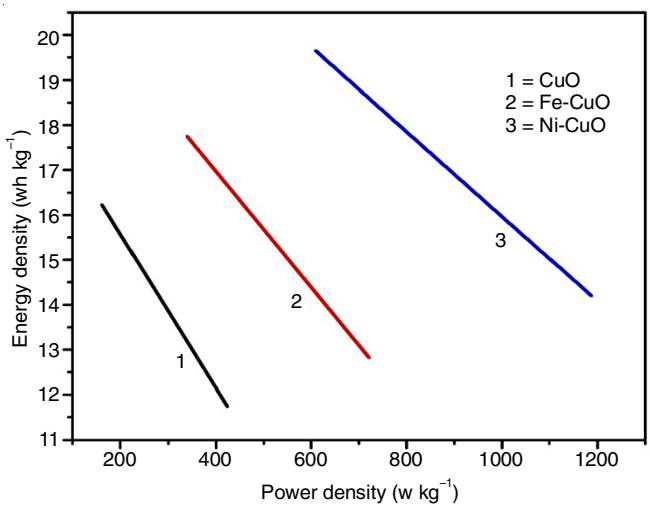

Fig. 10. Ragone plot for CuO, Fe-CuO and Ni-CuO nanoparticles

TABLE-4
POWER DENSITY AND ENERGY DENSITY VALUES OF CuO, Fe DOPED CuO AND Ni DOPED CuO

Component	5 A/g		10 A/g	
	Energy density (Wh/kg)	Power density (W/kg)	Energy density (Wh/kg)	Power density (W/kg)
CuO	16.22	161.68	11.74	424.12
Fe-CuO	17.75	339.79	12.82	720.79
Ni-CuO	19.65	609.69	14.2	1186.73

Fig. 11 shows the Nyquist plots of CuO, Fe-CuO and Ni-CuO electrodes, where a semi-circle region indicates the high frequency region, while the narrow straight line indicates the low frequency region. The low frequency region represents relatively vertical capacitive nature of the electrodes. The solution

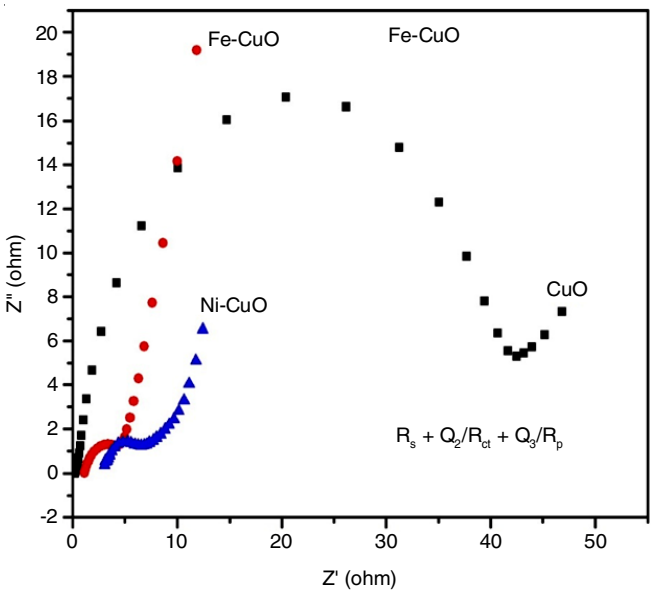

Fig. 11. Nyquist plots for CuO, Fe-CuO and Ni-CuO nanoparticles

resistance (R_{ct}) of the cell is calculated from the intercept between the impedance plot with the real impedance of Z′-axis. The electrochemical reaction on the electrode/electrolyte interface was relatively easier for Ni-CuO than the Fe-CuO and pure CuO electrodes. Thus, the R_p (Table-5) values obtained for the Ni-CuO electrode is comparatively lesser than the pure CuO and Fe-CuO electrodes.

TABLE-5
CHARGE TRANSFER RESISTANCE OF CuO, Fe-CuO AND Ni-CuO

Component	R_S (Ohm)	R_{ct} (Ohm)
CuO	2.465	39.50
Fe-CuO	1.431	9.42
Ni-CuO	1.101	7.61

The observed EIS values clearly show the supercilious capacitive behaviour of the Ni-CuO electrode than the pure CuO and Fe-CuO. A progressive decrease in the interface layer resistance and the charge transfer resistance on the surface were seen because of intercalation of Ni ion doped with CuO nanomaterials. Thus, the semi-circle for Ni-CuO (Fig. 11) electrode was shorter than Fe-CuO and pure CuO electrodes [45-48].

Conclusion

The CuO, Fe-CuO and Ni-CuO nanoparticles were successfully prepared by sol-gel method using NaOH as a mineralizer.

The XRD patterns revealed the presence of tetragonal crystal system of CuO, Fe-CuO, and Ni-CuO with a good crystallinity. The average crystalline size 33.72 nm (CuO), 21.49 nm (Fe-CuO) and 19.16 nm (Ni-CuO) were observed from the XRD results. The SEM images concluded the rod like shape with fine surface for pure CuO nanoparticles. Element colour mapping confirmed a good dispersion of Cu, Fe, Ni and O and the presence of elements alone signified the purity of the samples. The Cu-O, Fe-O and Ni-O vibrational bands were observed in the FT-IR confirmed the formation of bare and doped nanomaterials. The calculated band gap value of bare and the Fe, Ni doped CuO were 3.8, 3.5 and 3.7 eV respectively, and the XPS represents the principles of binding energy. The cyclic voltammetry shows that the prepared samples exhibited a quasi rectangular shape, which depicts the pseudocapacitance nature of the samples. The EIS spectra show that the Ni-CuO electrode exhibited the lower resistance value than the other electrodes. Hence, it is concluded that the prepared Ni-CuO electrode can be considered as the potential candidate for the supercapacitance applications.

CONFLICT OF INTEREST

The authors declare that there is no conflict of interests regarding the publication of this article.

REFERENCES

1. T. Huang, B. Liu, P. Yang, Z. Qiu and Z. Hu, *Int. J. Electrochem. Sci.*, **13**, 6144 (2018); https://doi.org/10.20964/2018.06.60
2. X. Zheng, H. Wang, C. Wang, Z. Deng, L. Chen, Y. Li, T. Hasan and B.L. Su, *Nano Energy*, **22**, 269 (2016); https://doi.org/10.1016/j.nanoen.2016.02.017
3. K. Adib, M. Rahimi-Nasrabadi, Z. Rezvani, S.M. Pourmortazavi, F. Ahmadi, H.R. Naderi and M.R. Ganjali, *J. Mater. Sci. Mater. Electron.*, **27**, 4541 (2016); https://doi.org/10.1007/s10854-016-4329-4
4. T. Arun, K. Prabakaran, R. Udayabhaskar, R.V. Mangalaraja and A. Akbari-Fakhrabadi, *Appl. Surf. Sci.*, **485**, 147 (2019); https://doi.org/10.1016/j.apsusc.2019.04.177
5. R.K. Mishra, G.W. Baek, K. Kim, H.I. Kwon and S.H. Jin, *J. Appl. Surf. Sci.*, **425**, 923 (2017); https://doi.org/10.1016/j.apsusc.2017.07.045
6. L. Fang, Y. Xie, Y. Wang, Z. Zhang, P. Liu, N. Cheng, J. Liu, Y. Tu, H. Zhao and J. Zhang, *J. Appl. Surf. Sci.*, **464**, 479 (2019); https://doi.org/10.1016/j.apsusc.2018.09.124
7. S.K. Shinde, M.B. Jalak, G.S. Ghodake, N.C. Maile, V.S. Kumbhar, D.S. Lee, V.J. Fulari and D.-Y. Kim, *Appl. Surf. Sci.*, **466**, 822 (2019); https://doi.org/10.1016/j.apsusc.2018.10.100
8. R.J. Deokate, R.S. Kalubarme, C.J. Park and C.D. Lokhande, *Electrochim. Acta*, **224**, 378 (2017); https://doi.org/10.1016/j.electacta.2016.12.034
9. S.I. Kim, J.H. Kang, S.W. Kim and J.H. Jang, *Nano Energy*, **39**, 639 (2017); https://doi.org/10.1016/j.nanoen.2017.07.050
10. R. Murugan, G. Ravi, G. Vijayaprasath, S. Rajendran, M. Nallappan, M. Thaiyan, M. Gopalan and Y. Hayakawa, *Phys. Chem. Chem. Phys.*, **19**, 4396 (2017); https://doi.org/10.1039/C6CP08281E
11. Y. Li, X. Hou, Z. Zhang, Z. Hai, H. Xu, D. Cui, S. Zhuiykov and C. Xue, *J. Appl. Surf. Sci*, **436**, 242 (2018); https://doi.org/10.1016/j.apsusc.2017.12.025
12. Z. Hai, M. Karbalaei Akbari, Z. Wei, C. Xue, H. Xu, S. Zhuiykov and J. Hu, *Electrochim. Acta*, **246**, 625 (2017); https://doi.org/10.1016/j.electacta.2017.06.095
13. S.K. Kannan and M. Sundrarajan, *Adv. Powder Technol.*, **26**, 1505 (2015); https://doi.org/10.1016/j.apt.2015.08.009
14. P. Suktha, N. Phattharasupakun, P. Dittanet and M. Sawangphruk, *RSC Adv.*, **7**, 9958 (2017); https://doi.org/10.1039/C6RA28499J
15. J. Liu, H. Yang and X. Xue, *CrystEngComm*, **21**, 1097 (2019); https://doi.org/10.1039/C8CE01920G
16. T. Li, H. Yu, L. Zhi, W. Zhang, L. Dang, Z. Liu and Z. Lei, *J. Phys. Chem. C*, **121**, 18982 (2017); https://doi.org/10.1021/acs.jpcc.7b04330
17. R. Khan, M. Habib, M.A. Gondal, A. Khalil, Z.U. Rehman, Z. Muhammad, Y.A. Haleem, C. Wang, C.Q. Wu and L. Song, *Mater. Res. Express*, **4**, 105501 (2017); https://doi.org/10.1088/2053-1591/aa8dc4
18. L. Ren, G. Zhang, Z. Yan, L. Kang, H. Xu, F. Shi, Z. Lei and Z. Liu, *Electrochim. Acta*, **231**, 705 (2017); https://doi.org/10.1016/j.electacta.2017.02.056
19. C.T. Meneses, J.G.S. Duque, L.G. Vivas and M. Knobel, *J. Non-Cryst. Solids*, **354**, 4830 (2008); https://doi.org/10.1016/j.jnoncrysol.2008.04.025
20. M. Nasir, N. Patra, M.A. Ahmed, D.K. Shukla, D. Bhattacharya, S. Kumar, C.L. Prajapat, D.M. Phase, S.N. Jha, S. Biring and S. Sen, *RSC Adv.*, **7**, 31970 (2017); https://doi.org/10.1039/C7RA03960C
21. Y. Gulen, F. Bayansal, B. Sahin, H.A. Cetinkara and H.S. Guder, *Ceram. Int.*, **39**, 6475 (2013); https://doi.org/10.1016/j.ceramint.2013.01.077
22. H.D. Colorado and G.A. Perez Alcazar, *Hyperfine Interact.*, **202**, 139 (2011); https://doi.org/10.1007/s10751-011-0354-0
23. R. Suresh, K. Tamilarasan and D.S. Vadivu, *J. Ovonic Res.*, **12**, 215 (2016).
24. S. Manna and S.K. De, *J. Magn. Magn. Mater.*, **322**, 2749 (2010); https://doi.org/10.1016/j.jmmm.2010.04.020
25. S.Y. Yin, S.L. Yuan, Z.M. Tian, L. Liu, C.H. Wang, X.F. Zheng, H.N. Duan and S.X. Huo, *J. Appl. Phys.*, **107**, 043909 (2010); https://doi.org/10.1063/1.3294618
26. D.T. Gazioglu, F. Dumludag, A. Altindal, A. Angelopoulos and T. Fildisis, *AIP Conf. Proc.*, **1203**, 456 (2010); https://doi.org/10.1063/1.3322487
27. D. Li, Y.H. Leung, A.B. Djurišiæ, Z.T. Liu, M.H. Xie, J. Gao and W.K. Chan, *J. Cryst. Growth*, **282**, 105 (2005); https://doi.org/10.1016/j.jcrysgro.2005.04.090
28. C. Thangamani, M. Ponnar, P. Priyadharshini, P. Monisha, S.S. Gomathi and K. Pushpanathan, *Surf. Rev. Lett.*, **26**, 1850184 (2019); https://doi.org/10.1142/S0218625X18501846
29. P. Rani, A. Gupta, S. Kaur, V. Singh, S. Kumar and D. Kumar, *AIP Conf. Proc.*, **1728**, 020057 (2016); https://doi.org/10.1063/1.4946108
30. S. Al-Amri, M. Ansari, S. Rafique, M. Aldhahri, S. Rahimuddin, A. Azam and A. Memic, *Curr. Nanosci.*, **11**, 191 (2015); https://doi.org/10.2174/1573413710666141024212856
31. P. Mallick and R. Biswal, *Nanosci. Nanotechnol.*, **6**, 59 (2016); https://Doi.org/10.5923/J.nn.20160604.01
32. K.C. Barick, P. Sharma, A. Mukhija, J.K. Sainis, A. Gupta and P.A. Hassan, *J. Environ. Chem. Eng.*, **3**, 1346 (2015); https://doi.org/10.1016/j.jece.2014.12.007
33. F.M. Pontes, D.S.L. Pontes, A.J. Chiquito, M.A. Pereira-da-Silva and E. Longo, *Mater. Lett.*, **138**, 179 (2015); https://doi.org/10.1016/j.matlet.2014.10.005
34. J.W. Ha, J. Oh, H. Choi, H. Ryu, W.J. Lee and J.S. Bae, *J. Ind. Eng. Chem.*, **58**, 38 (2018); https://doi.org/10.1016/j.jiec.2017.09.004
35. S. Nithya, R. Sharan, M. Roy, H. Kim, T. Ishihara and A. Dutta, *Mater. Res. Bull.*, **118**, 110478 (2019); https://doi.org/10.1016/j.materresbull.2019.05.003
36. L. Martín-García, I. Bernal-Villamil, M. Oujja, E. Carrasco, R. Gargallo-Caballero, M. Castillejo, J.F. Marco, S. Gallego and J. De la Figuera, *J. Mater. Chem. C Mater. Opt. Electron. Dev.*, **4**, 1850 (2016); https://doi.org/10.1039/C5TC03871E

37. P.T. Babar, A.C. Lokhande, M.G. Gang, B.S. Pawar, S.M. Pawar and J.H. Kim, *J. Ind. Eng. Chem.*, **60**, 493 (2018); https://doi.org/10.1016/j.jiec.2017.11.037
38. R. Sivakami, S.G. Babu, S. Dhanuskodi and R. Karvembu, *RSC Adv.*, **5**, 8571 (2015); https://doi.org/10.1039/C4RA13256D
39. V.K. Premkumar, G. Sivakumar, S. Dinesh and S. Barathan, *J. Mater. Sci. Mater. Electron.*, **28**, 4780 (2017); https://doi.org/10.1007/s10854-016-6123-8
40. V.K. Premkumar and G. Sivakumar, *J. Mater. Sci. Mater. Electron.*, **28**, 14226 (2017); https://doi.org/10.1007/s10854-017-7280-0
41. D. Govindarajan, V. Uma Shankar and R. Gopalakrishnan, *J. Mater. Sci. Mater. Electron.*, **30**, 16142 (2019); https://doi.org/10.1007/s10854-019-01984-9
42. D.P. Dubal, G.S. Gund, C.D. Lokhande and R. Holze, *Mater. Res. Bull.*, **48**, 923 (2013); https://doi.org/10.1016/j.materresbull.2012.11.081
43. M. Ates, A. Garip, O. Yörük, Y. Bayrak, O. Kuzgun and M. Yildirim, *Plast. Rubber Compos.*, **48**, 168 (2019); https://doi.org/10.1080/14658011.2019.1588509
44. L. Arun, C. Karthikeyan, D. Philip, M. Sasikumar, E. Elanthamilan, J.P. Merlin and C. Unni, *J. Mater. Sci. Mater. Electron.*, **29**, 21180 (2018); https://doi.org/10.1007/s10854-018-0268-6
45. M. Huang, F. Li, Y.X. Zhang, B. Li and X. Gao, *Ceram. Int.*, **40**, 5533 (2014); https://doi.org/10.1016/j.ceramint.2013.10.143
46. M. Aghazadeh, M.G. Maragheh and P. Norouzi, *Int. J. Electrochem. Sci.*, **13**, 1355 (2018); https://doi.org/10.20964/2018.02.40
47. J. Ye, Z. Li, Z. Dai, Z. Zhang, M. Guo and X. Wang, *J. Electron. Mater.*, **45**, 4237 (2016); https://doi.org/10.1007/s11664-016-4587-1
48. V. Senthilkumar, Y.S. Kim, S. Chandrasekaran, B. Rajagopalan, E.J. Kim and J.S. Chung, *RSC Adv.*, **5**, 20545 (2015); https://doi.org/10.1039/C5RA00035A